

UniRGB-IR: A Unified Framework for RGB-Infrared Semantic Tasks via Adapter Tuning

Maoxun Yuan*, Bo Cui*, Tianyi Zhao, Jiayi Wang, Shan Fu[‡] and Xingxing Wei[‡]

Abstract—Semantic analysis on visible (RGB) and infrared (IR) images has gained attention for its ability to be more accurate and robust under low-illumination and complex weather conditions. Due to the lack of pre-trained foundation models on the large-scale infrared image datasets, existing methods prefer to design task-specific frameworks and directly fine-tune them with pre-trained foundation models on their RGB-IR semantic relevance datasets, which results in poor scalability and limited generalization. In this work, we propose a general and efficient framework called UniRGB-IR to unify RGB-IR semantic tasks, in which a novel adapter is developed to efficiently introduce richer RGB-IR features into the pre-trained RGB-based foundation model. Specifically, our framework consists of a RGB-based foundation model, a Multi-modal Feature Pool (MFP) module and a Supplementary Feature Injector (SFI) module. The MFP and SFI modules cooperate with each other as an adapter to effectively complement the RGB-based features with the rich RGB-IR features. During training process, we freeze the entire foundation model to inherit prior knowledge and only optimize the proposed adapter. Furthermore, to verify the effectiveness of our framework, we utilize the vanilla vision transformer (ViT-Base) as the pre-trained foundation model to perform extensive experiments. Experimental results on various RGB-IR downstream tasks demonstrate that our method can achieve state-of-the-art performance. The source code and results are available at <https://github.com/PoTtsui99/UniRGB-IR.git>

Index Terms—RGB-IR Semantic Tasks, Multi-modal Fusion, Adapter, Vision Transformer.

I. INTRODUCTION

Image semantic analysis in the visible images is a common practice in computer vision and has been widely used in a variety of vision tasks [1]–[3]. However, visible cameras have proved to be difficult in providing reliable imaging [4], [5], due to their limited bandwidth across the spectrum. Particularly under low-illumination conditions and adverse weather scenarios, RGB images suffer from limited informative content. Therefore, infrared (IR) modality with stronger low-light adaptability is used as additional information to supplement RGB modality [4], [6]. Afterwards, the joint use of RGB and IR images has been applied in more and more semantic analysis tasks.

Maoxun Yuan and Bo Cui are with the Beijing Key Laboratory of Digital Media, School of Computer Science and Engineering, Beihang University, Beijing 100191, China (email: yuanmaoxun@buaa.edu.cn).

Tianyi Zhao is with the Institute of Artificial Intelligence, Beihang University, No.37, Xueyuan Road, Haidian District, Beijing, 100191, China.

Jiayi Wang and Shan Fu are with China Academy of Information & Communications Technology, Beijing, China.

Xingxing Wei is with Institute of Artificial Intelligence, Hangzhou Innovation Institute, Beihang University, Beijing, 100191, China (email: xxwei@buaa.edu.cn).

[‡] indicates the corresponding author.

* represents the equal contribution to this work.

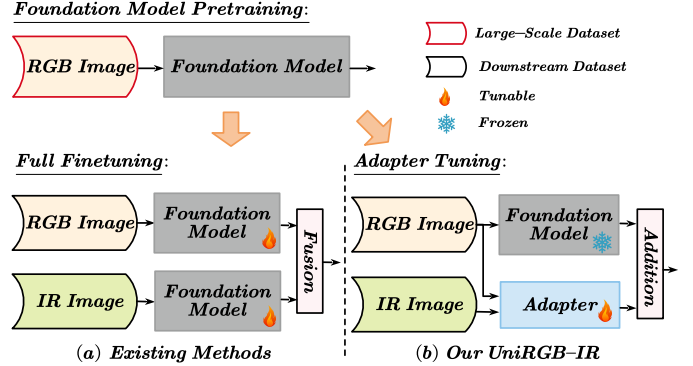


Fig. 1. Existing full fine-tuning methods vs. our UniRGB-IR framework. (a) Existing methods use pre-trained RGB-based foundation models and fully fine-tune them on their RGB-IR semantic relevance datasets. (b) We utilize the Adapter [13] to propose a new unified framework called UniRGB-IR, which can efficiently introduce richer RGB-IR features into the pre-trained foundation model for downstream tasks.

With the rapid advancements in physical computing capabilities, more and more general-purpose foundation backbones [7], [8] pre-trained on large-scale RGB-based datasets (e.g., ImageNet [9] and COCO [10]) have been designed for various tasks. Since these pre-trained base models implicitly encode a lot of prior knowledge, it is believed that pre-trained models can promote the improvement of downstream task performance and speed up training convergence. Therefore, fine-tuning the pre-trained foundation models [11], [12] on their semantic relevance datasets has become a common paradigm to improve the performance on specific downstream tasks.

However, due to the lack of pre-trained foundation models on the large-scale infrared image datasets, for RGB-Infrared semantic tasks, a straightforward and prevailing way [14], [15] is to use pre-trained RGB-based models and fine-tune them on their RGB-IR semantic relevance datasets as shown in Figure 1 (a). For example, RGB-IR object detectors [14], [16] utilize RGB-based models as strong baselines and fine-tune them to extract RGB and IR features. SwinNet [17] is explored based on the RGB-based transformer to extract hierarchical features of each modality for the detection of salient RGB-IR objects. Similarly, Ha *et al.* [18] establish a novel baseline by incorporating infrared modality features into an RGB-based framework and fine-tune it on the RGB-IR semantic segmentation benchmark. Among the efforts to achieve competitive results, these approaches still suffer from two major issues:

(1) Different semantic tasks require customized model structures, resulting in poor model versatility and excessive parameter storage.

(2) Full fine-tuning strategy impairs the prior knowledge encoded in the foundation model, which limits the generalization potential of the fine-tuned foundation model.

Above challenges necessitate the adaptation of RGB-based foundation models to construct a unified framework capable of handling RGB-IR semantic tasks effectively.

Drawing inspiration from recent advances in adapters [13], [19], which are initially used to yield an extensible model to effectively exploit the potential representation of foundation models in the natural language processing (NLP) field, we develop an adapter to dynamically introduce richer RGB-IR features into the pre-trained RGB-based foundation model. In our adapter, a feature extractor is designed to obtain rich RGB-IR features and a feature injector is proposed to adaptively introduce the required features for the foundation model. Without modifying the original RGB-based foundation model, the powerful pre-trained weights can be directly frozen to accelerate training convergence and achieve efficient fine-tuning on downstream tasks. Therefore, in this paper, we propose an efficient and universal foundation model for RGB-IR semantic tasks. In particular, we are the first to construct a **Unified framework for RGB-IR semantic tasks**, called **UniRGB-IR**, as shown in Figure 1 (b).

Specifically, we design two core modules in our UniRGB-IR: a **Multi-modal Feature Pool** module (MFP) and a **Supplementary Feature Injector** module (SFI). In the MFP module, the multi-receptive field convolution and the feature pyramid are deployed to capture contextual multi-scale features from RGB and IR images. These features are fused at different scales to complement foundation models for different RGB-IR semantic tasks. For the SFI module, a cross-attention mechanism is used to dynamically inject the required features into the pre-trained foundation model, which facilitates our UniRGB-IR framework with a robust feature representation ability. To inherit prior knowledge of the foundation model pre-trained on large-scale datasets, we utilize the adapter tuning paradigm instead of the full fine-tuning manner. We freeze the entire pre-trained weights and only optimize our proposed adapter. Consequently, UniRGB-IR can serve as a unified framework to achieve effective fine-tuning for various RGB-IR semantic tasks.

Overall, our contributions are summarized as follows:

- We explore an efficient and universal framework called UniRGB-IR for RGB-IR semantic tasks. To the best of our knowledge, this is the first attempt to construct a unified framework for RGB-IR downstream tasks.
- We design a Multi-modal Feature Pool module and a Supplementary Feature Injector module. The former extracts contextual multi-scale features from two modality images, and the latter dynamically injects the required features into the pre-trained model. These two modules can be efficiently fine-tuned with adapter tuning paradigm to complement the pre-trained foundation model with richer RGB-IR features for RGB-IR semantic tasks.
- We incorporate the vision transformer foundation model into the UniRGB-IR framework to evaluate the effectiveness of our method on RGB-IR downstream tasks, including RGB-IR object detection, RGB-IR semantic

segmentation, and RGB-IR salient object detection. Extensive experimental results demonstrate that our methods can efficiently achieve superior performance on these RGB-IR downstream tasks.

The remainder of the article is organized as follows. In the Section II, we review the scientific literature related to our proposed approach. Section III introduces our proposed UniRGB-IR for RGB-Infrared semantic tasks. Experimental results are presented in Section IV, along with the comparison with state-of-the-art methods. Finally, we conclude with a discussion of our contribution in Section VI.

II. RELATED WORK

A. Vision Foundation Models

Recently, thanks to the powerful long-distance modeling capability, vision transformers (ViT) [7] have been widely used as the foundation model in many vision tasks to achieve competitive results. The original ViT is a plain, non-hierarchical structure for image classification. Based on it, ViTDet [20] also constructs a non-hierarchical model by incorporating the feature pyramid. However, the non-hierarchical structure lacks rich feature representation, resulting in unsatisfactory performance. Subsequently, various hierarchical transformers [8], [21]–[23] have been proposed for different downstream vision tasks. Swin Transformer [21] and Multiscale Vision Transformer [22] are designed based on the ViT model to explore multi-scale features to improve the performance of image classification and object detection tasks. Besides, PVT [24] performs global attention on the downsampled key and value maps for dense prediction. In this paper, we also introduce the ViT model as the pre-trained foundation model to construct a unified framework for RGB-IR semantic tasks.

B. RGB-IR Semantic Tasks

RGB-IR Object Detection. Zhang *et al.* [25] explore a two-stream SSD [26] structure to capture the contextual enhanced features for RGB-IR object detection. Besides, AR-CNN [27] is presented based on faster R-CNN [28] to align RGB and IR features. With the emergence of transformers, Yuan *et al.* [29] propose a complementary fusion transformer (CFT) module to achieve advanced detection results. Furthermore, C²Former [5] is a novel transformer block and can be incorporated into existing pre-trained models to increase intra- and inter-modality feature representations.

RGB-IR Semantic Segmentation. MFNet [18] is proposed to incorporate infrared features into the RGB-based framework to perform RGB-IR semantic segmentation. Based on the transformer structure, Wu *et al.* [30] propose a novel CCFFNet to excavate complementary modality features for RGB-IR semantic segmentation. Moreover, CMX [31] is designed as a universal cross-modal fusion framework for RGB-IR semantic segmentation in an interactive fusion manner.

RGB-IR Salient Object Detection. SwinNet [17] is designed based on the Swin Transformer to extract hierarchical information of each modality, which achieves impressive results. CAVER [32] introduces the transformer to rethink the bi-modal salient object detection from a sequence-to-sequence

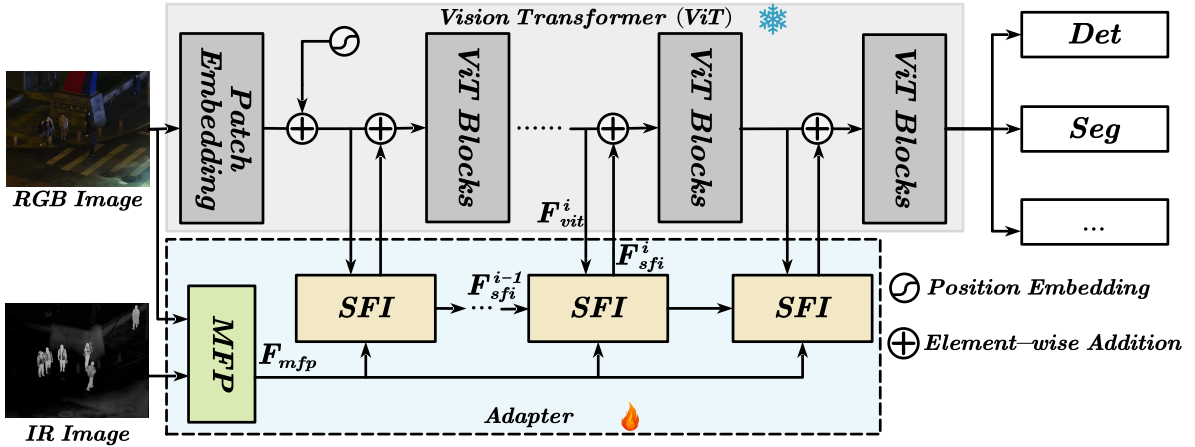


Fig. 2. The overall architecture of our UniRGB-IR. In our framework, a ViT model with different numbers of ViT blocks is deployed as a foundation model, which is divided into N (usually $N = 4$) stages for feature interaction. Besides, a Multi-modal Feature Pool (MFP) is designed to extract contextual multi-scale RGB-IR features and a Supplementary Feature Injector (SFI) is explored to introduce these features into the ViT foundation model. During training, we freeze the entire ViT model weights and only optimize the MFP and SFI modules.

perspective, which increases the model interpretability. Recently, Zhou *et al.* [33] transfer a large amount of knowledge learned in the transformer-based network to lightweight WaveNet through the distillation method.

The above methods attempt to design task-oriented structures to improve performance on corresponding downstream tasks. They either train the designed model from scratch or adopt a full fine-tuning strategy on a pre-trained model. Unlike these methods, we take a further step and deploy an adapter based on the pre-trained foundation model to unify the RGB-IR semantic tasks.

C. Adapter

In the NLP field, Adapter [13] first fixes the original foundation backbone and introduces new modules into the transformer for task-specific fine-tuning, thereby effectively adapting the pre-trained backbone to downstream NLP tasks. Afterwards, Adapter has been widely studied in computer vision. ViT-Adapter [34] and Low-Rank Adapter [35] are designed to introduce a modest number of trainable parameters into the ViT and fine-tuning efficiently for dense prediction tasks. In addition, PC-Adapter [36] explores an attention-based adapter to preserve global shape knowledge for domain adaptation on point cloud data. Recently, Adapter is also used as a parameter-efficient training technology for vision-and-language tasks [37], [38].

In this paper, we aim to explore an adapter capable of converting the IR features into the RGB features to fit the pre-trained foundation model, which remains challenging to design this unified framework. Our UniRGB-IR is the first to propose utilizing adapter to unify RGB-IR downstream tasks.

III. METHOD

A. Overall Architecture

The overall framework of UniRGB-IR is illustrated in Figure 2, which consists of three parts: vision transformer model, Multi-modal Feature Pool (MFP) module, and Supplementary

Feature Injector (SFI) module. In our framework, the ViT model is utilized as the pre-trained foundation model and frozen during the training process. Specifically, for the ViT model, the RGB image is directly fed into the patch embedding process to obtain the D -dimensional feature tokens, which are usually $1/16$ of the original image resolution. To complement the richer features required for various RGB-IR downstream tasks, we feed the RGB and IR images into the MFP module to extract contextual multi-scale features from two modalities (eg. $1/8$, $1/16$ and $1/32$ of the original image resolution). Afterwards, these richer features are dynamically injected into the features of ViT model through the SFI module, which can adaptively introduce the required RGB-IR features into the ViT model. To fully integrate the extracted features into the ViT model, we add the SFI module at the beginning of each stage. Thus, after N stages of feature injection, the final features from ViT model can be leveraged for various RGB-IR downstream tasks.

B. Multi-modal Feature Pool

To complement the rich feature representations for different RGB-IR downstream tasks, we introduce a multi-modal feature pool (MFP) module, including multiple perception and feature pyramid. The former can extract the contextual features with different convolution kernels, which achieve the long-distance modeling capability of CNNs. Different from existing works [39], [40] that increase the width or depth of the model, we efficiently achieve multi-receptive field perception in the channel dimension. As for feature pyramid, it can obtain multi-scale features to enhance the small object features. Thus, these two operations are connected in series to construct MFP module, as shown in Figure 3.

Specifically, for the input RGB ($H \times W \times 3$) and IR ($H \times W$) images, we first employ a stem block borrowed from ResNet to extract two modality features F_1^{rgb} and $F_1^{ir} \in \mathbb{R}^{H/4 \times W/4 \times C}$. Then, these two features are split into four equal parts by utilizing the channel splitting technique [41]. To extract multi-receptive field perception, each part is subjected to convolution

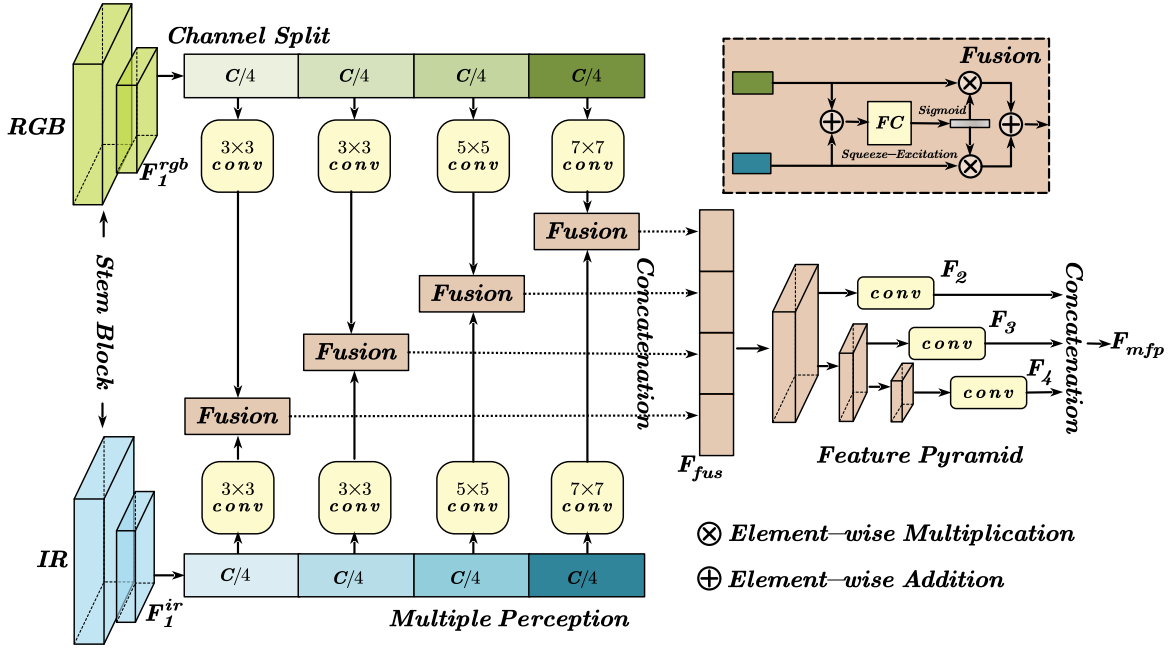


Fig. 3. Structure of the multi-modal feature pool (MFP) module. We explore the multiple perceptions to expand the receptive field of contextual feature extraction and utilize the feature pyramid to obtain the multi-scale features. In this module, Squeeze-Excitation(SE) attention is utilized to fuse two modality features. Thus, the contextual multi-scale features can be provided for the various RGB-IR downstream tasks.

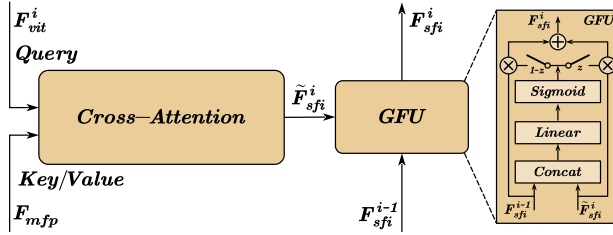


Fig. 4. Structure of supplementary feature injector (SFI) module. A gated fusion unit (GFU) is utilized to dynamically fuse the current and the last injected features.

operations with different kernel sizes (3×3 , 3×3 , 5×5 and 7×7). Then, we fuse each processed feature from two modalities by using a SE attention module (shown in Figure 3). Therefore, we concatenate each fused part to obtain RGB-IR contextual features F_{fus} . The above process can be represented as:

$$F_{fus} = \Gamma_{k=1}^4 (Fusion(W_k^{rgb} * f_k^{rgb}, W_k^{ir} * f_k^{ir})), \quad (1)$$

where $F_{fus} \in \mathbb{R}^{H/4 \times W/4 \times C}$, f_k^{rgb} and f_k^{ir} are the k -th part of F_1^{rgb} and F_1^{ir} features respectively, W_k is the convolution with k -th kernel size, Γ is the concatenation operation.

For the feature pyramid, a stack of three 3×3 convolutions with $stride = 2$ is conducted to downsample the size of the feature maps. Then, features of each scale are fed into a 1×1 convolution to project the feature maps to D dimensions. Therefore, we can obtain a set of multi-scale features $\{F_2, F_3, F_4\}$ with $1/8$, $1/16$, and $1/32$ of the original image resolution, respectively. Finally, we flatten and concatenate these features into feature tokens $F_{mfp} \in \mathbb{R}^{(\frac{HW}{8^2} + \frac{HW}{16^2} + \frac{HW}{32^2}) \times D}$, which will be used as supplementary features for the ViT model.

C. Supplementary Feature Injector

As shown in Figure 4, we propose a supplementary feature injector (SFI) module to adaptively introduce the contextual multi-scale features without altering the ViT structure. Since the sequence lengths of contextual multi-scale features F_{mfp} and the ViT features F_{vit}^i are different, to address this, we employ sparse attention (eg. [42] and [43]) to dynamically sample supplementary features from each scale. To be specific, we utilize the ViT features $F_{vit}^i \in \mathbb{R}^{\frac{HW}{16^2} \times D}$ as the query, and the contextual multi-scale features $F_{mfp} \in \mathbb{R}^{(\frac{HW}{8^2} + \frac{HW}{16^2} + \frac{HW}{32^2}) \times D}$ as the key and value:

$$\tilde{F}_{sfi}^i = Attention(LN(F_{vit}^i), LN(F_{mfp})), \quad (2)$$

where $Attention(\cdot)$ is the attention layer and $LN(\cdot)$ is Layer-Norm [44] which is intended to reduce modality discrepancy. Furthermore, we adopt progressive injection to introduce contextual multi-scale features, which can balance the foundation model features and the injected features F_{sfi}^i . Thus, a gated fusion unit is explored to predict the fusion weight z to gate F_{sfi}^{i-1} and \tilde{F}_{sfi}^i for dynamic fusion. Specifically, we concatenate the two features F_{sfi}^{i-1} and \tilde{F}_{sfi}^i and feed it into linear layer to predict the weight z . Then, z and $1-z$ are used to fuse F_{sfi}^{i-1} and \tilde{F}_{sfi}^i features respectively. The final output features F_{sfi}^i of SFI module can be formulated as:

$$F_{sfi}^i = \begin{cases} \tilde{F}_{sfi}^i, & i = 1 \\ GFU(\tilde{F}_{sfi}^i, F_{sfi}^{i-1}), & i = 2 \dots N \end{cases} \quad (3)$$

where $GFU(\cdot, \cdot)$ is the gated fusion unit shown in Figure 4.

TABLE I

COMPARISON RESULTS (mAP, IN%) ON THE FLIR AND LLVIP DATASET. THE BEST RESULTS ARE HIGHLIGHTED IN **RED** AND THE SECOND-BEST ARE HIGHLIGHTED IN **BLUE**. “-” INDICATES THAT THE AUTHOR DID NOT PROVIDE THE CORRESPONDING RESULTS.

Methods	Modality	FLIR			LLVIP		
		mAP	mAP ₅₀	mAP ₇₅	mAP	mAP ₅₀	mAP ₇₅
SSD [26]	IR	24.6	57.0	18.0	53.5	90.2	57.9
RetinaNet [45]	IR	31.5	66.1	25.3	55.1	94.8	57.6
Faster R-CNN [28]	IR	37.6	75.8	31.6	54.5	94.6	57.6
Cascade R-CNN (ViT-B) [46]	IR	41.9	78.6	37.3	60.4	94.9	67.5
DDQ-DETR [47]	IR	37.1	73.9	32.2	58.6	93.9	64.6
SSD [26]	RGB	18.8	46.3	13.1	39.8	82.6	31.8
RetinaNet [45]	RGB	21.9	51.2	15.2	42.8	88.0	34.4
Faster R-CNN [28]	RGB	27.7	62.2	21.2	45.1	87.0	41.2
Cascade R-CNN (ViT-B) [46]	RGB	33.3	69.3	26.2	51.7	90.3	54.7
DDQ-DETR [47]	RGB	30.9	64.9	24.5	46.7	86.1	45.8
GAFF [48]	RGB+IR	37.4	74.6	31.3	55.8	94.0	60.2
ProbEn [49]	RGB+IR	37.9	75.5	31.8	51.5	93.4	50.2
LGADet [50]	RGB+IR	-	74.5	-	-	-	-
CSAA [51]	RGB+IR	41.3	79.2	37.4	59.2	94.3	66.6
UniRGB-IR (Ours)	RGB+IR	44.1	81.4	40.2	63.2	96.1	72.2

TABLE II

COMPARISON RESULTS (MR⁻², IN%) UNDER ‘ALL-DATASET’ SETTINGS OF DIFFERENT PEDESTRIAN DISTANCES, OCCLUSION LEVELS, AND LIGHT CONDITIONS (DAY AND NIGHT) ON THE KAIST DATASET. THE BEST AND SECOND RESULTS ARE HIGHLIGHTED IN **RED** AND **BLUE** RESPECTIVELY.

Methods	Near	Medium	Far	None	Partial	Heavy	Day	Night	All
ACF [52]	28.74	53.67	88.20	62.94	81.40	88.08	64.31	75.06	67.74
Halfway Fusion [53]	8.13	30.34	75.70	43.13	65.21	74.36	47.58	52.35	49.18
FusionRPN+BF [54]	0.04	30.87	88.86	47.45	56.10	72.20	52.33	51.09	51.70
IAF R-CNN [55]	0.96	25.54	77.84	40.17	48.40	69.76	42.46	47.70	44.23
IATDNN+IASS [56]	0.04	28.55	83.42	45.43	46.25	64.57	49.02	49.37	48.96
CIAN [25]	3.71	19.04	55.82	30.31	41.57	62.48	36.02	32.38	35.53
MSDS-R-CNN [57]	1.29	16.19	63.73	29.86	38.71	63.37	32.06	38.83	34.15
AR-CNN [27]	0.00	16.08	69.00	31.40	38.63	55.73	34.36	36.12	34.95
MBNet [58]	0.00	16.07	55.99	27.74	35.43	59.14	32.37	30.95	31.87
TSFADet [16]	0.00	15.99	50.71	25.63	37.29	65.67	31.76	27.44	30.74
CMPD [59]	0.00	12.99	51.22	24.04	33.88	59.37	28.30	30.56	28.98
CAGTDet [29]	0.00	14.00	49.40	24.48	33.20	59.35	28.79	27.73	28.96
C ² Former [5]	0.00	13.71	48.14	23.91	32.84	57.81	28.48	26.67	28.39
UniRGB-IR (Ours)	0.00	13.44	38.21	20.26	31.67	55.03	25.93	23.95	25.21

D. Adapter Tuning Paradigm

To fully inherit the prior knowledge of the ViT pre-trained on large-scale datasets, we explore the adapter tuning paradigm instead of the full fine-tuning manner. For the dataset $D = \{(x_j, gt_j)\}_{j=1}^M$ of the downstream task, full fine-tuning process calculates the loss between the prediction and the ground truth, which can be formulated as:

$$\mathcal{L}(D, \theta) = \sum_{j=1}^M \text{loss}(F_{\theta}(x_j), gt_j), \quad (4)$$

where loss represents the loss function and F_{θ} denotes the entire network parameterized by θ . Afterwards, θ is optimized through the formula:

$$\theta \leftarrow \arg \min_{\theta} \mathcal{L}(D, \theta). \quad (5)$$

However, in our adapter tuning paradigm, the parameter θ consists of two parts, one part is the parameter in the original ViT model θ_V , and the other part is the parameter in our UniRGB-IR θ_A . During training, we freeze the parameter θ_V

and only optimize the parameter θ_A . Thus, the loss function and optimization of our a can be represented as:

$$\mathcal{L}(D, \theta_V, \theta_A) = \sum_{j=1}^M \text{loss}(F_{\theta_V, \theta_A}(x_j), gt_j), \quad (6)$$

$$\theta_A \leftarrow \arg \min_{\theta_A} \mathcal{L}(D, \theta_V, \theta_A). \quad (7)$$

IV. OBJECT DETECTION AND SEMANTIC SEGMENTATION

To evaluate the effectiveness of our UniRGB-IR, we utilize the ViT-Base model (pre-trained on COCO [10] dataset) as the foundation model and utilize this framework to perform different RGB-IR semantic tasks. During training, we freeze the ViT-Base model and only optimize the MFP and SFI modules. We evaluate and compare our method with various competitive models, including CNN-based and Transformer-based models. Besides, our evaluation spans various tasks, including RGB-IR object detection on FLIR [69], LLVIP [70], and KAIST [52] datasets, RGB-IR semantic segmentation on MFNet [18] and PST9000 [62] datasets. Furthermore,

TABLE III
RESULTS ON THE PST900 DATASET. THE BEST RESULTS ARE HIGHLIGHTED IN RED AND THE SECOND-BEST ARE HIGHLIGHTED IN BLUE.
“-” INDICATES THAT THE AUTHOR DID NOT PROVIDE THE CORRESPONDING RESULTS.

Methods	Background		Fire-Extinguisher		Backpack		Hand-Drill		Survivor		mAcc	mIoU
	Acc	IoU	Acc	IoU	Acc	IoU	Acc	IoU	Acc	IoU		
MFNet [18]	99.9	98.7	71.8	67.4	52.8	52.4	46.7	39.3	18.8	18.9	58.0	55.3
RTFNet [60]	99.9	99.0	78.6	54.8	62.5	60.8	76.7	61.0	65.2	62.5	76.6	67.6
CCNet [61]	99.6	98.7	88.1	73.8	76.0	73.0	54.1	51.0	49.5	33.5	73.46	66.0
PSTNet [62]	-	98.9	-	70.1	-	69.2	-	53.6	-	50.0	-	68.4
ACNet [63]	99.8	99.3	84.9	60.0	85.6	83.2	53.6	51.5	69.1	65.2	78.7	71.8
FDCNet [64]	99.7	99.2	91.8	71.5	77.5	72.2	82.5	70.4	78.4	72.4	86.0	77.1
CGFNet [65]	99.7	99.3	96.3	71.7	87.6	82.0	70.5	59.7	86.3	77.4	88.1	78.0
EGFNet [66]	99.5	99.2	95.2	71.3	94.2	83.1	98.0	64.7	83.3	74.3	94.0	78.5
CCFFNet [30]	99.9	99.4	87.0	79.3	80.2	77.8	88.3	77.4	77.9	73.4	86.7	81.5
RSFNet [67]	-	99.4	-	75.4	-	84.9	-	72.9	-	70.1	-	80.5
SGFNet [68]	99.8	99.4	89.4	75.6	90.4	85.4	94.0	76.7	82.7	76.7	91.2	82.8
UniRGB-IR (Ours)	99.7	99.5	97.0	72.0	93.3	87.7	95.5	78.0	86.1	77.8	94.3	82.8

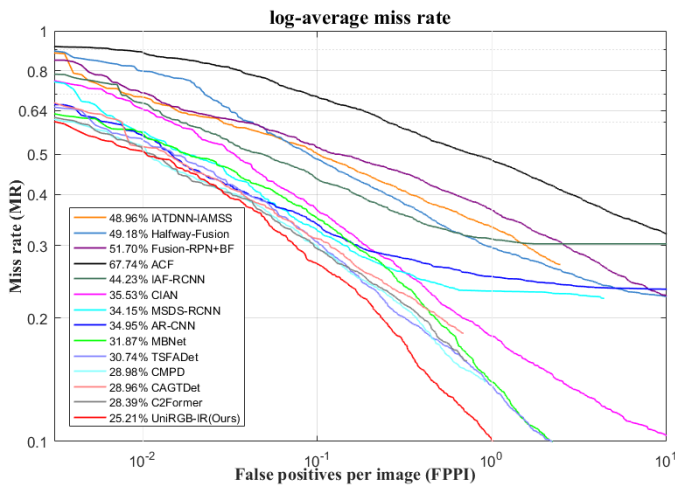


Fig. 5. The Miss rate curves for all detectors are plotted against False Positives Per Image (FPPI) under the IoU threshold of 0.5 on the KAIST dataset.

ablation experiments on the designed modules and qualitative experiments are also conducted to verify that the UniRGB-IR framework can be leveraged as a unified framework to efficiently introduce IR features into the foundation model to achieve superior performance.

A. RGB-IR Object Detection

Datasets. Our object detection experiments are based on the three paired RGB and IR object detection datasets. FLIR [69] is a paired visible and infrared object detection dataset, including daytime and night scenes, which has 4,129 aligned RGB-IR image pairs for training and 1,013 for testing. For LLVIP [70] dataset, it contains 15,488 aligned RGB-IR image pairs, of which 12,025 images are used for training and 3,463 images for testing. As for KAIST [52] dataset, it is a aligned multispectral pedestrian detection dataset, in which 8,963 and 2,252 image pairs are utilized for training and testing.

Metrics. For FLIR and LLVIP datasets, we employ mean Average Precision (mAP) to evaluate the detection performance. As for KAIST dataset, we use log-average miss rate MR over the false positive per image (FPPI) with the range of $[10^{-2}, 10^0]$ to evaluate the pedestrian detection performance.

Settings. All the experiments are conducted with NVIDIA GeForce RTX 3090 GPUs. We implement our framework on the MMDetection library and use the Cascade R-CNN as the basic framework to perform RGB-IR object detection. The detector is trained with an initial learning rate of 2×10^{-4} for 48 epochs. The batch size is set to 16, and the AdamW optimizer is employed with a weight decay of 0.1. Horizontal flipping is also used for data augmentation.

Results on FLIR and LLVIP datasets. We compare our method with five common mono-modality methods and four competitive multi-modality methods. As shown in Table I, it can be seen that most of the multi-modality detectors are even worse than mono-modality detectors (eg. Faster R-CNN in IR modality). Since the RGB feature interfere with infrared feature under limited illumination conditions, it has a negative impact on the fused features utilized for object detection tasks. However, our UniRGB-IR can effectively solve this problem through the SFI module, enabling the detector to achieve better classification and localization processes.

Results on KAIST dataset. The quantitative results of the different methods on the KAIST dataset are shown in Table II. The experiments are conducted under ‘All-dataset’ settings [52]. We compare our UniRGB-IR with thirteen multi-modal object detection methods. Our model achieves the best performance on the ‘All’, ‘Day’, and ‘Night’ conditions and the other four of five subsets (‘Near’, ‘Far’, ‘None’, ‘Partial’ and ‘Heavy’), and rank second in the ‘Medium’ subset. Furthermore, our detector surpasses the previous best competitor C²Former by 3.18% on the ‘All’ condition, which indicates UniRGB-IR is robust to the complex scenes. Intuitively, we draw the log-average Miss Rate (MR) over the False Positive Per Image (FPPI) curve of these detectors as shown in Figure 5. All these results verify that our UniRGB-IR can exploit the potential representation from the RGB-based foundation model to achieve superior results.

B. RGB-IR Semantic Segmentation

Datasets. Our semantic segmentation experiments are performed on the two public RGB-IR semantic segmentation datasets: PST900 [62] and MFNet [18]. The PST900 dataset is divided into 597 pairs for training and 288 pairs for testing,

TABLE IV
RESULTS ON THE MFNET DATASET. THE BEST RESULTS ARE HIGHLIGHTED IN RED AND THE SECOND-BEST ARE HIGHLIGHTED IN BLUE.
“-” INDICATES THAT THE AUTHOR DID NOT THE CORRESPONDING RESULTS.

Methods	Unlabeled		Car		Person		Bike		Curve		Car Stop		Guardrail		Color Cone		Bump		mAcc	mIoU
	Acc	IoU																		
MFNet [18]	98.7	96.9	77.2	65.9	67.0	58.9	53.9	42.9	36.2	29.9	12.5	9.9	0.1	0.0	30.3	25.2	30.0	27.7	45.1	39.7
RTFNet [60]	99.4	98.5	93.0	87.4	79.3	70.3	76.8	62.7	60.7	45.3	38.5	29.8	0.0	0.0	45.5	29.1	74.7	55.7	63.1	53.2
PSTNet [62]	98.8	97.4	89.4	77.0	74.8	67.2	65.8	50.8	42.5	35.2	34.6	25.2	0.0	0.0	32.7	29.9	61.1	55.0	55.5	48.6
FuseSeg [71]	99.0	97.6	93.1	87.9	81.4	71.7	78.5	64.6	68.4	44.8	29.1	22.7	63.7	6.4	55.8	46.9	66.4	47.9	70.6	54.5
ABMDRNet [72]	98.6	97.8	94.3	84.4	90.0	69.6	75.7	60.3	64.0	45.1	44.1	33.1	31.0	5.1	61.7	47.4	66.2	50.0	69.5	54.8
MFFNet [73]	99.3	97.8	91.4	87.1	82.6	74.4	76.7	61.3	58.7	45.6	44.9	30.6	60.0	5.2	64.4	57.0	72.7	40.5	72.3	55.5
EGFNet [66]	98.7	98.0	95.8	87.6	89.0	69.8	80.6	58.8	71.5	42.8	48.7	33.8	33.6	7.0	65.3	8.3	71.1	47.1	72.7	54.8
MTANet [74]	98.4	98.0	95.8	88.1	90.9	71.5	80.3	60.7	75.3	40.9	62.8	38.9	38.7	13.7	63.8	45.9	70.8	47.2	75.2	56.1
MLFNet [75]	-	97.3	-	82.3	-	68.1	-	67.3	-	27.3	-	30.4	-	15.7	-	55.6	-	40.1	-	53.8
FEANet [76]	99.3	98.2	93.3	87.8	82.7	71.1	76.7	61.1	65.5	46.5	26.6	22.1	70.8	6.6	66.6	55.4	77.3	48.9	73.2	55.3
GMNet [77]	99.2	97.5	94.1	86.5	83.0	73.1	76.9	61.7	59.7	44.0	55.0	42.3	71.2	14.5	54.7	48.7	73.1	47.4	74.1	57.3
CCFFNet [30]	98.8	98.3	94.5	89.6	83.6	74.2	73.2	63.1	67.2	50.5	38.7	31.9	30.6	4.8	55.2	49.7	72.9	56.3	68.3	57.6
CCAFFMNet [78]	97.4	95.2	95.0	88.6	86.1	72.9	82.1	67.1	71.2	45.9	32.1	24.8	57.1	17.8	58.0	50.1	76.2	57.8	72.8	57.8
CMX [31]	-	98.3	-	89.4	-	74.8	-	64.7	-	47.3	-	30.1	-	8.1	-	52.4	-	59.4	-	58.2
FDCNet [64]	98.8	98.2	94.1	87.5	91.4	72.4	78.1	61.7	70.1	43.8	34.4	27.2	61.5	7.3	64.0	52.0	74.5	56.6	74.1	56.3
ECGFNet [79]	99.3	97.5	89.4	83.5	85.2	72.1	72.9	61.6	62.8	40.5	44.8	30.8	45.2	11.1	57.2	49.7	65.1	50.9	69.1	55.3
LASNet [80]	97.6	97.4	94.9	84.2	81.7	67.1	82.1	56.9	70.7	41.1	56.8	39.6	59.5	18.9	58.1	48.8	77.2	40.1	75.4	54.9
UniRGB-IR (Ours)	98.3	97.2	94.0	83.7	88.7	64.9	88.0	69.8	53.3	36.8	58.5	41.0	69.7	36.7	77.6	56.2	55.2	47.3	75.7	59.3

TABLE V
ABLATION STUDIES OF KEY COMPONENTS ON THE FLIR AND PST900 DATASETS. THE BEST RESULTS ARE HIGHLIGHTED IN BOLD.

MFP	SFI	FLIR			PST900	
		mAP	mAP ₅₀	mAP ₇₅	mAcc	mIoU
		39.6	76.3	35.9	90.1	77.5
✓		41.2	77.9	36.5	91.7	78.8
✓	✓	44.1	81.4	40.2	94.3	82.8

containing five categories (background, fire extinguisher, backpack, hand drill, and survivor). The MFNet dataset provides 1,569 pairs and contains nine classes (Car, Curve, Person, Guardrail, Car stop, Bike, Bump, Color cone, and Background). The dataset is divided into three parts: training, verification and testing according to the ratio of 2:1:1.

Metrics. Two metrics are utilized to evaluate the performance of semantic segmentation, namely mean accuracy (mAcc) and mean intersection over union (mIoU). Both metrics are calculated by averaging the ratios of the intersection and union of all categories.

Settings. Similarly, as the RGB-IR object detection task, we incorporate our method into the SETR [81] basic framework and implement it on the MMSegmentation library. The fine-tuning process spins a total of 10K iterations with an initial learning rate of 0.01. We employ the SGD optimizer and set the batch size to 16.

Results. The quantitative results of the different RGB-IR segmentation methods on the PST900 and MFNet dataset are shown in Table III and Table IV respectively. The comparison results show that our model significantly outperforms other methods. Specifically, our model obtains the best performance in terms of both the mAcc and mIoU. In PST900 dataset, our model performs competitive performance in the Backpack, Hand-Drill and Survivor, outperforming the second-best methods by 2.3%, 0.6% and 0.4% IoU, respectively. In predicting

TABLE VI
ABLATION OF ADDING SFI MODULE TO DIFFERENT STAGES.

Different Stages with SFI module				mAP	mAP ₅₀	mAP ₇₅
Stage 1	Stage 2	Stage 3	Stage 4			
✓				41.7	80.0	37.2
✓	✓			43.3	81.6	39.7
✓	✓	✓		44.1	81.4	40.2
✓	✓	✓	✓	42.7	79.9	38.2

TABLE VII
ABLATION OF THE DIFFERENT ATTENTION MECHANISMS.

Attention Mechanism	Complexity	mAP	mAP ₅₀	mAP ₇₅
Global Attention [82]	Quadratic	36.1	72.8	30.6
Pale Attention [42]	Linear	31.6	68.4	24.6
Deformable Attention [43]	Linear	44.1	81.4	40.2

Color Cone class on MFNet dataset, our model achieves the first and second best in terms of both evaluation metrics, with about 11% Acc higher than that of the second-best. These results show that our UniRGB-IR can also be used flexibly for segmentation tasks without any modification, which validates the universality of our method.

C. Ablation Study

Ablation for components. To investigate the contribution of the SFI and MFP modules, we gradually add each module to the baseline model as shown in Table V. We stack RGB and IR images and feed them into the Cascade R-CNN detector and SETR framework (ViT backbone) for full fine-tuning on the corresponding tasks, which are considered as our baseline models. Then, we freeze the ViT model and introduce the MFP module to extract contextual multi-scale features (element-wise addition), which results in 1.6% mAP and 1.3% mIoU improvements. Finally, we replace the element-wise addition

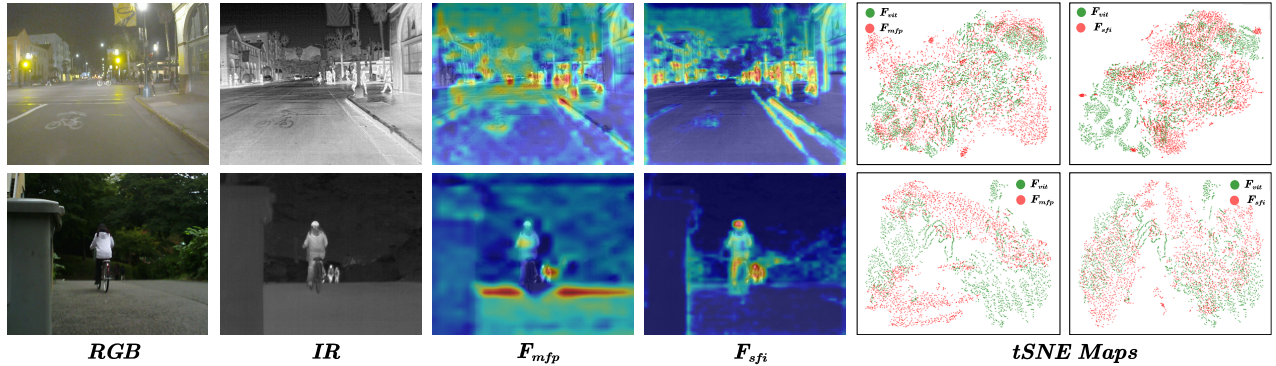


Fig. 6. Visualization of intermediate results. The F_{mfp} and F_{sfi} features from the first stage are visualized in the third and fourth columns. The tSNE visualizations are also shown in the last two columns.

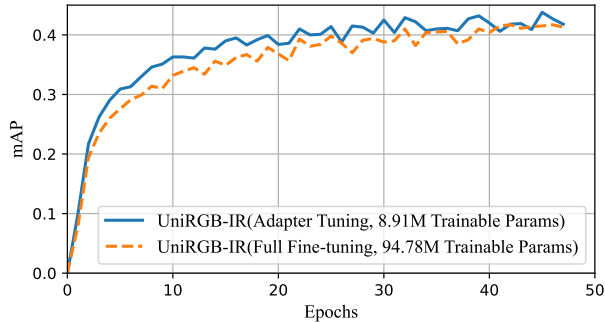


Fig. 7. Training efficiency analysis on the FLIR dataset.

operation with the SFI module and further improve the mAP and mIoU metrics by 2.9% and 4.0% respectively, which achieve the best performance on both datasets.

SFI module at different stages. We add the SFI module to the ViT pre-trained model at the beginning of different stages. From Table VI, we can find that by adding the SFI module at the first stage, the detector achieves 41.7% mAP on FLIR dataset. After adding the SFI module in the second and third stages, the performance further improved by about 2% and 3% mAP, respectively. However, continuing to add it to the final stage will reduce the detection performance while also increasing computational overhead. Therefore, we add the SFI module from the first stage to the third stage of ViT model.

Attention type in SFI module. Since the attention mechanism in our SFI module is replaceable, we adopt three popular attention mechanisms in our UniRGB-IR to discuss their impact on model performance. As shown in Table VII, the detector achieves the best performance with linear complexity by utilizing deformable attention. Thus, the deformable attention is more suitable for our framework and utilized as the default configuration. It is worth noting that it can be replaced by other attention mechanisms to further achieve superior performance.

D. Visualization Analysis

Intermediate results. To illustrate the effectiveness of the SFI module, we visualize the intermediate results on the FLIR dataset. From F_{mfp} and F_{sfi} in Figure 6, we can find that the foreground objects in the F_{sfi} become salient through

the SFI module. Furthermore, we also visualize the tSNE maps of $F_{mfp}-F_{vit}$ and $F_{sfi}-F_{vit}$ respectively. After using the SFI module, the distribution of injected features F_{sfi} is more concentrated than the distribution of ViT features F_{vit} , indicating that the required richer RGB-IR features can be well supplemented into the ViT model through the SFI module.

Training efficiency. We further plot the mAP curves for each epoch of UniRGB-IR with different training paradigm to demonstrate the efficiency of UniRGB-IR, as shown in Figure 7. During the training process, all hyperparameters of the two models are the same. From Figure 7, we can find that the convergence speed of the adapter tuning paradigm surpasses that of the full fine-tuning strategy. Moreover, by utilizing the adapter tuning paradigm, our UniRGB-IR achieves superior performance with a smaller number of trainable parameters (about 10% of the full fine-tuning model). The above results verify the efficiency of our method.

V. TASK EXTENSION

A. RGB-IR Salient Object Detection

Datasets. RGB-IR salient object detection (SOD) experiments are performed on the three public datasets: VT821 [87], VT1000 [89] and VT5000 [92]. The VT821 dataset includes 821 registered RGB and IR images. The VT1000 dataset contains 1000 registered RGB-IR images with simple scenes and aligned images. The VT5000 dataset is a recent large-scale RGB-IR dataset, including a full-day scene under various limited light conditions. As usual in [92], we utilize 2500 image pairs in the VT5000 dataset as the training dataset, and the remaining image pairs along with the image pairs from the VT821 and VT1000 datasets are used as the test datasets.

Metrics. Four metrics are utilized to evaluate the performance of salient object detection namely F-measure ($adpF \uparrow$), E-Measure ($adpE \uparrow$), S-Measure ($S \uparrow$) and Mean absolute error ($MAE \downarrow$). \uparrow and \downarrow denote the higher the better and the lower the better, respectively.

Settings. As same as the RGB-IR semantic segmentation task, we incorporate our method into the SETR basic framework and also implement it on the MMSegmentation library. The fine-tuning process spins a total of 10K iterations with an initial learning rate of 0.01. We use the SGD optimizer and set the

TABLE VIII

QUANTITATIVE COMPARISON OF RGB-IR SALIENT OBJECT DETECTION TASK ON VT821, VT1000 AND VT5000 DATASETS. * REPRESENTS RGB-D SOD TRANSFORMED INTO RGB-T SOD. THE BEST RESULTS ARE HIGHLIGHTED IN RED AND THE SECOND-BEST ARE HIGHLIGHTED IN BLUE.

Model	VT821				VT1000				VT5000			
	$S \uparrow$	$adpE \uparrow$	$adpF \uparrow$	$MAE \downarrow$	$S \uparrow$	$adpE \uparrow$	$adpF \uparrow$	$MAE \downarrow$	$S \uparrow$	$adpE \uparrow$	$adpF \uparrow$	$MAE \downarrow$
MMCI* [83]	0.763	0.784	0.618	0.087	0.886	0.892	0.803	0.039	0.827	0.859	0.714	0.055
TANet* [84]	0.818	0.852	0.717	0.052	0.902	0.912	0.838	0.030	0.847	0.883	0.754	0.047
S2MA* [85]	0.811	0.813	0.709	0.098	0.918	0.912	0.848	0.029	0.853	0.864	0.743	0.053
JLDCF* [86]	0.839	0.830	0.726	0.076	0.912	0.899	0.829	0.030	0.861	0.860	0.739	0.050
MTMR [87]	0.725	0.815	0.662	0.109	0.706	0.836	0.715	0.119	0.680	0.795	0.595	0.114
M3S-NIR [88]	0.723	0.859	0.734	0.140	0.726	0.827	0.717	0.145	0.652	0.780	0.575	0.168
SGDL [89]	0.765	0.847	0.731	0.085	0.787	0.856	0.764	0.090	0.750	0.824	0.672	0.089
FMSF [90]	0.760	0.796	0.640	0.080	0.873	0.899	0.823	0.037	0.814	0.864	0.734	0.055
MIDD [91]	0.871	0.895	0.803	0.033	0.915	0.933	0.880	0.027	0.868	0.896	0.799	0.043
ADF [92]	0.810	0.842	0.717	0.077	0.910	0.921	0.847	0.034	0.864	0.891	0.778	0.048
LSNet [93]	0.877	0.911	0.827	0.033	0.924	0.936	0.887	0.022	0.876	0.916	0.827	0.036
UniRGB-IR (Ours)	0.881	0.895	0.806	0.039	0.939	0.943	0.894	0.018	0.906	0.935	0.849	0.027

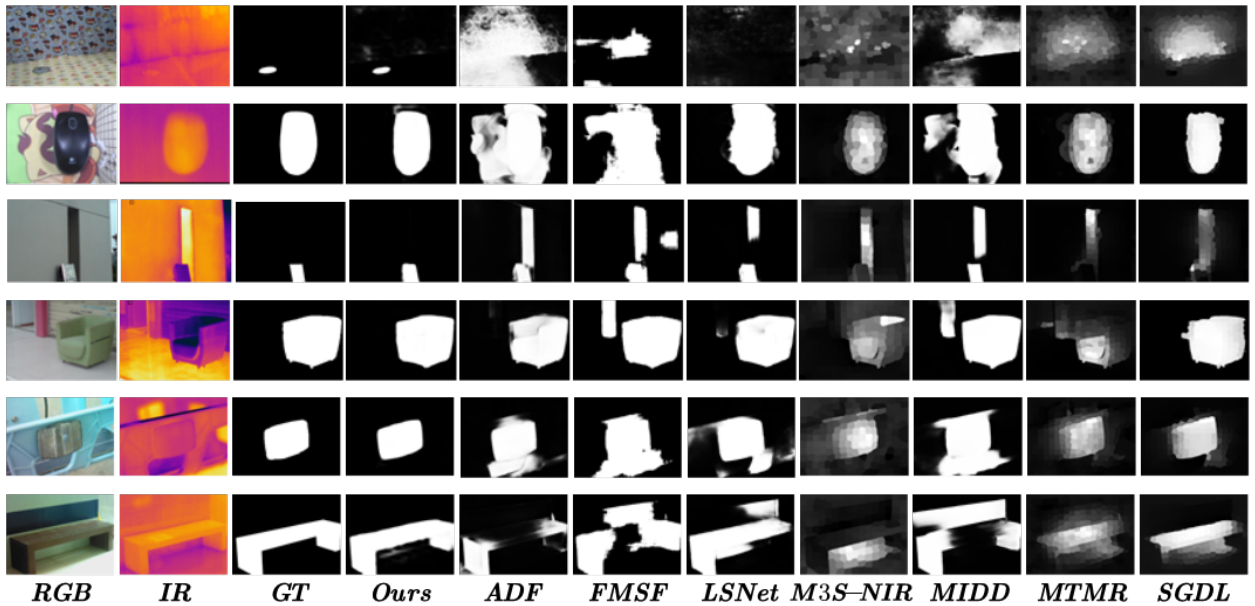


Fig. 8. Saliency maps of proposed UniRGB-IR and seven representative SOTA RGB-IR SOD methods in difference scenes. From top to bottom are visualization examples from the VT821, VT1000 and VT5000 datasets respectively.

batch size to 64. For convenience, all input images are resized to 224×224 for testing.

Quantitative Comparison. Table VIII reports the quantitative comparison results. As can be seen from Table VIII, our UniRGB-IR outperforms SOTA methods both on VT1000 and VT5000 datasets in all evaluation metrics. Specifically, the S , $adpE$, $adpF$ and MAE matrices of our UniRGB-IR achieve 0.906, 0.935, 0.849 and 0.027 on VT5000, all of which are higher than the previous competitor LSNet [93]. These remarkable results clearly indicate that the saliency maps predicted by UniRGB-IR are close to the corresponding ground-truths, which verifies the effectiveness of our method.

Qualitative Evaluation. Qualitative RGB-IR SOD comparisons are shown in Figure 8. The first and third rows show scenes containing small objects. The second and fifth rows show the salient object with the complex backgrounds. All these scenes are suitably handled by our UniRGB-IR, which verifies that UniRGB-IR is more effective while providing

high-quality results with appropriate detection capabilities.

B. RGB-IR Face Recognition

Datasets. The face recognition task is performed on the IRIS thermal/visible face dataset [94], which contains pairs of thermal and visible face images captured simultaneously under different illumination conditions and pose rotations as shown in Figure 9. The dataset has a total of 4228 pairs of thermal and visible images from 30 subjects. We randomly select 80% of the images as the training set and the rest as the test set to verify our method.

Metrics. For RGB-IR face recognition task, we utilize two metrics to evaluate the recognition results, called Rank-1 accuracy and True Positive Rate (TPR) at False Acceptance Rate (FAR) of 1% and 0.1%. Rank-1 accuracy is defined as the proportion of correctly predicted face image pairs (True positive) among the total number of image pairs and TPR at

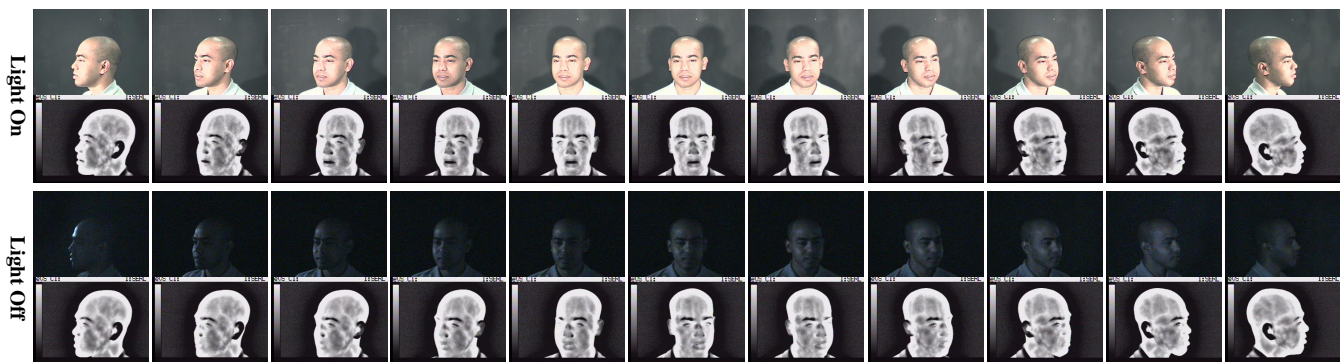


Fig. 9. Example of visible and infrared images from IRIS face dataset. Each subject in the dataset contains different pose rotations and illumination conditions.

TABLE IX
QUANTITATIVE COMPARISON OF RGB-IR FACE RECOGNITION TASK ON
IRIS THERMAL/VISIBLE FACE DATASET.

Methods	Modality	Rank-1(%)	TPR@FAR	
			= 1%	= 0.1%
Arcface [95]	IR	70.4	80.2	53.9
Adaface [96]	IR	76.3	85.1	62.3
Arcface [95]	RGB	61.6	75.7	49.2
Adaface [96]	RGB	64.6	79.6	52.7
Arcface+UniRGB-IR (Ours)	RGB+IR	83.3	88.5	65.8
Adaface+UniRGB-IR (Ours)	RGB+IR	84.2	89.4	66.2

an FAR is described as the number of correct predictions at a specific percentage of acceptable false predictions.

Settings. We conduct the RGB-IR face recognition experiments based on the Insightface [95] library and incorporate our method into the framework to replace the backbone network. During training, the images are resized to a size of 224×224 pixels and the labels contain class information only. At this stage, the categorical cross-entropy loss is used for multimodal face recognition. The training process is terminated at 20 epochs and the learning rate is initialized as 1×10^{-4} with SGD optimizer and divided by 10 at 10, 14, 17 epochs.

Results. Table IX presents the rank-1 identification and verification rates on IRIS thermal/visible face dataset. It can be seen from the table that the recognition results in the IR modality are obviously better than those in the RGB modality. Besides, after using our UniRGB-IR framework, the recognition performance is further improved. Specifically, Our UniRGB-IR with Adaface achieves 84.3%, 89.4% and 66.2% in Rank-1, TPR@FAR = 1% and TPR@FAR = 0.1% respectively, which are the highest among these results.

VI. CONCLUSION

In this paper, we proposed an efficient and universal framework (named UniRGB-IR) for RGB-IR semantic tasks. Our framework contains a Multi-modal Feature Pool module and a Supplementary Feature Injector module. The former extracts contextual multi-scale features from two modality images, and the latter adaptively injects the features into the transformer model. These two modules can be efficiently optimized to complement the pre-trained foundation model with richer

RGB-IR features. To evaluate the effectiveness of our method, we incorporated the ViT-Base model into the framework as the pre-trained foundation model and performed various RGB-IR downstream tasks. Extensive experiments verify that our UniRGB-IR can be effectively leveraged as a unified framework for RGB-IR semantic tasks. We believe that our framework holds potential for expansion to a broader range of multi-modal tasks.

REFERENCES

- [1] A. Khan, A. Sohail, U. Zahoora, and A. S. Qureshi, "A survey of the recent architectures of deep convolutional neural networks," *Artificial intelligence review*, vol. 53, pp. 5455–5516, 2020.
- [2] H. Yan, B. Li, H. Zhang, and X. Wei, "An antijamming and lightweight ship detector designed for spaceborne optical images," *IEEE Journal of Selected Topics in Applied Earth Observations and Remote Sensing*, vol. 15, pp. 4468–4481, 2022.
- [3] L. Bo, X. Xiaoyang, W. Xingxing, and T. Wenting, "Ship detection and classification from optical remote sensing images: A survey," *Chinese Journal of Aeronautics*, vol. 34, no. 3, pp. 145–163, 2021.
- [4] D. Xu, W. Ouyang, E. Ricci, X. Wang, and N. Sebe, "Learning cross-modal deep representations for robust pedestrian detection," in *Proceedings of the IEEE conference on computer vision and pattern recognition*, 2017, pp. 5363–5371.
- [5] M. Yuan and X. Wei, "C2former: Calibrated and complementary transformer for rgb-infrared object detection," *IEEE Transactions on Geoscience and Remote Sensing*, pp. 1–1, 2024.
- [6] T. Zhao, M. Yuan, and X. Wei, "Removal and selection: Improving rgb-infrared object detection via coarse-to-fine fusion," *arXiv preprint arXiv:2401.10731*, 2024.
- [7] A. Dosovitskiy, L. Beyer, A. Kolesnikov, D. Weissenborn, X. Zhai, T. Unterthiner, M. Dehghani, M. Minderer, G. Heigold, S. Gelly *et al.*, "An image is worth 16x16 words: Transformers for image recognition at scale," *arXiv preprint arXiv:2010.11929*, 2020.
- [8] C. Xia, X. Wang, F. Lv, X. Hao, and Y. Shi, "Vit-comer: Vision transformer with convolutional multi-scale feature interaction for dense predictions," *arXiv preprint arXiv:2403.07392*, 2024.
- [9] J. Deng, W. Dong, R. Socher, L.-J. Li, K. Li, and L. Fei-Fei, "Imagenet: A large-scale hierarchical image database," in *2009 IEEE conference on computer vision and pattern recognition*. Ieee, 2009, pp. 248–255.
- [10] T.-Y. Lin, M. Maire, S. Belongie, J. Hays, P. Perona, D. Ramanan, P. Dollár, and C. L. Zitnick, "Microsoft coco: Common objects in context," in *Computer Vision—ECCV 2014: 13th European Conference, Zurich, Switzerland, September 6–12, 2014, Proceedings, Part V 13*. Springer, 2014, pp. 740–755.
- [11] X. Wei, Y. Huang, Y. Sun, and J. Yu, "Unified adversarial patch for visible-infrared cross-modal attacks in the physical world," *IEEE Transactions on Pattern Analysis and Machine Intelligence*, 2023.
- [12] Y. Shi, F. Lv, X. Wang, C. Xia, S. Li, S. Yang, T. Xi, and G. Zhang, "Open-transmind: A new baseline and benchmark for 1st foundation model challenge of intelligent transportation," in *Proceedings of the IEEE/CVF Conference on Computer Vision and Pattern Recognition*, 2023, pp. 6327–6334.

- [13] N. Houlsby, A. Giurgiu, S. Jastrzebski, B. Morrone, Q. De Laroussilhe, A. Gesmundo, M. Attariyan, and S. Gelly, "Parameter-efficient transfer learning for nlp," in *International conference on machine learning*. PMLR, 2019, pp. 2790–2799.
- [14] L. Zhang, Z. Liu, X. Zhu, Z. Song, X. Yang, Z. Lei, and H. Qiao, "Weakly aligned feature fusion for multimodal object detection," *IEEE Transactions on Neural Networks and Learning Systems*, 2021.
- [15] L. Liu, J. Chen, H. Wu, G. Li, C. Li, and L. Lin, "Cross-modal collaborative representation learning and a large-scale rgbt benchmark for crowd counting," in *Proceedings of the IEEE/CVF conference on computer vision and pattern recognition*, 2021, pp. 4823–4833.
- [16] M. Yuan, Y. Wang, and X. Wei, "Translation, scale and rotation: cross-modal alignment meets rgb-infrared vehicle detection," in *European Conference on Computer Vision*. Springer, 2022, pp. 509–525.
- [17] Z. Liu, Y. Tan, Q. He, and Y. Xiao, "Swinnet: Swin transformer drives edge-aware rgb-d and rgb-t salient object detection," *IEEE Transactions on Circuits and Systems for Video Technology*, vol. 32, no. 7, pp. 4486–4497, 2021.
- [18] Q. Ha, K. Watanabe, T. Karasawa, Y. Ushiku, and T. Harada, "Mfnnet: Towards real-time semantic segmentation for autonomous vehicles with multi-spectral scenes," in *2017 IEEE/RSJ International Conference on Intelligent Robots and Systems (IROS)*. IEEE, 2017, pp. 5108–5115.
- [19] A. C. Stickland and I. Murray, "Bert and pals: Projected attention layers for efficient adaptation in multi-task learning," in *International Conference on Machine Learning*. PMLR, 2019, pp. 5986–5995.
- [20] Y. Li, H. Mao, R. Girshick, and K. He, "Exploring plain vision transformer backbones for object detection," in *European Conference on Computer Vision*. Springer, 2022, pp. 280–296.
- [21] Z. Liu, Y. Lin, Y. Cao, H. Hu, Y. Wei, Z. Zhang, S. Lin, and B. Guo, "Swin transformer: Hierarchical vision transformer using shifted windows," in *Proceedings of the IEEE/CVF international conference on computer vision*, 2021, pp. 10 012–10 022.
- [22] H. Fan, B. Xiong, K. Mangalam, Y. Li, Z. Yan, J. Malik, and C. Feichtenhofer, "Multiscale vision transformers," in *Proceedings of the IEEE/CVF international conference on computer vision*, 2021, pp. 6824–6835.
- [23] F. Li, H. Zhang, H. Xu, S. Liu, L. Zhang, L. M. Ni, and H.-Y. Shum, "Mask dino: Towards a unified transformer-based framework for object detection and segmentation," in *Proceedings of the IEEE/CVF Conference on Computer Vision and Pattern Recognition*, 2023, pp. 3041–3050.
- [24] W. Wang, E. Xie, X. Li, D.-P. Fan, K. Song, D. Liang, T. Lu, P. Luo, and L. Shao, "Pyramid vision transformer: A versatile backbone for dense prediction without convolutions," in *Proceedings of the IEEE/CVF international conference on computer vision*, 2021, pp. 568–578.
- [25] L. Zhang, Z. Liu, S. Zhang, X. Yang, H. Qiao, K. Huang, and A. Husain, "Cross-modality interactive attention network for multispectral pedestrian detection," *Information Fusion*, vol. 50, pp. 20–29, 2019.
- [26] W. Liu, D. Anguelov, D. Erhan, C. Szegedy, S. Reed, C.-Y. Fu, and A. C. Berg, "Ssd: Single shot multibox detector," in *Computer Vision—ECCV 2016: 14th European Conference, Amsterdam, The Netherlands, October 11–14, 2016, Proceedings, Part I 14*. Springer, 2016, pp. 21–37.
- [27] L. Zhang, X. Zhu, X. Chen, X. Yang, Z. Lei, and Z. Liu, "Weakly aligned cross-modal learning for multispectral pedestrian detection," in *Proceedings of the IEEE/CVF international conference on computer vision*, 2019, pp. 5127–5137.
- [28] S. Ren, K. He, R. Girshick, and J. Sun, "Faster r-cnn: Towards real-time object detection with region proposal networks," *Advances in neural information processing systems*, vol. 28, 2015.
- [29] M. Yuan, X. Shi, N. Wang, Y. Wang, and X. Wei, "Improving rgb-infrared object detection with cascade alignment-guided transformer," *Information Fusion*, vol. 105, p. 102246, 2024.
- [30] W. Wu, T. Chu, and Q. Liu, "Complementarity-aware cross-modal feature fusion network for rgb-t semantic segmentation," *Pattern Recognition*, vol. 131, p. 108881, 2022.
- [31] J. Zhang, H. Liu, K. Yang, X. Hu, R. Liu, and R. Stiefelhagen, "Cmx: Cross-modal fusion for rgb-x semantic segmentation with transformers," *IEEE Transactions on Intelligent Transportation Systems*, 2023.
- [32] Y. Pang, X. Zhao, L. Zhang, and H. Lu, "Caver: Cross-modal view-mixed transformer for bi-modal salient object detection," *IEEE Transactions on Image Processing*, vol. 32, pp. 892–904, 2023.
- [33] W. Zhou, F. Sun, Q. Jiang, R. Cong, and J.-N. Hwang, "Wavenet: Wavelet network with knowledge distillation for rgb-t salient object detection," *IEEE Transactions on Image Processing*, 2023.
- [34] Z. Chen, Y. Duan, W. Wang, J. He, T. Lu, J. Dai, and Y. Qiao, "Vision transformer adapter for dense predictions," *arXiv preprint arXiv:2205.08534*, 2022.
- [35] D. Yin, Y. Yang, Z. Wang, H. Yu, K. Wei, and X. Sun, "1% vs 100%: Parameter-efficient low rank adapter for dense predictions," in *Proceedings of the IEEE/CVF Conference on Computer Vision and Pattern Recognition*, 2023, pp. 20 116–20 126.
- [36] J. Park, H. Seo, and E. Yang, "Pc-adapter: Topology-aware adapter for efficient domain adaption on point clouds with rectified pseudo-label," in *Proceedings of the IEEE/CVF International Conference on Computer Vision*, 2023, pp. 11 530–11 540.
- [37] Y.-L. Sung, J. Cho, and M. Bansal, "Vl-adapter: Parameter-efficient transfer learning for vision-and-language tasks," in *Proceedings of the IEEE/CVF Conference on Computer Vision and Pattern Recognition*, 2022, pp. 5227–5237.
- [38] U. Upadhyay, S. Karthik, M. Mancini, and Z. Akata, "Provlm: Probabilistic adapter for frozen vision-language models," in *Proceedings of the IEEE/CVF International Conference on Computer Vision*, 2023, pp. 1899–1910.
- [39] Z. He, Y. Cao, L. Du, B. Xu, J. Yang, Y. Cao, S. Tang, and Y. Zhuang, "Mrfn: Multi-receptive-field network for fast and accurate single image super-resolution," *IEEE Transactions on Multimedia*, vol. 22, no. 4, pp. 1042–1054, 2019.
- [40] X. Wu, D. Hong, and J. Chanussot, "Uiu-net: U-net in u-net for infrared small object detection," *IEEE Transactions on Image Processing*, vol. 32, pp. 364–376, 2022.
- [41] N. Ma, X. Zhang, H.-T. Zheng, and J. Sun, "Shufflenet v2: Practical guidelines for efficient cnn architecture design," in *Proceedings of the European conference on computer vision (ECCV)*, 2018, pp. 116–131.
- [42] S. Wu, T. Wu, H. Tan, and G. Guo, "Pale transformer: A general vision transformer backbone with pale-shaped attention," in *Proceedings of the AAAI Conference on Artificial Intelligence*, vol. 36, no. 3, 2022, pp. 2731–2739.
- [43] X. Zhu, W. Su, L. Lu, B. Li, X. Wang, and J. Dai, "Deformable detr: Deformable transformers for end-to-end object detection," *arXiv preprint arXiv:2010.04159*, 2020.
- [44] J. L. Ba, J. R. Kiros, and G. E. Hinton, "Layer normalization," *arXiv preprint arXiv:1607.06450*, 2016.
- [45] T.-Y. Lin, P. Goyal, R. Girshick, K. He, and P. Dollár, "Focal loss for dense object detection," in *Proceedings of the IEEE international conference on computer vision*, 2017, pp. 2980–2988.
- [46] Z. Cai and N. Vasconcelos, "Cascade r-cnn: Delving into high quality object detection," in *Proceedings of the IEEE conference on computer vision and pattern recognition*, 2018, pp. 6154–6162.
- [47] S. Zhang, X. Wang, J. Wang, J. Pang, C. Lyu, W. Zhang, P. Luo, and K. Chen, "Dense distinct query for end-to-end object detection," in *Proceedings of the IEEE/CVF conference on computer vision and pattern recognition*, 2023, pp. 7329–7338.
- [48] H. Zhang, E. Fromont, S. Lefèvre, and B. Avignon, "Guided attentive feature fusion for multispectral pedestrian detection," in *Proceedings of the IEEE/CVF winter conference on applications of computer vision*, 2021, pp. 72–80.
- [49] Y.-T. Chen, J. Shi, Z. Ye, C. Mertz, D. Ramanan, and S. Kong, "Multimodal object detection via probabilistic ensembling," in *European Conference on Computer Vision*. Springer, 2022, pp. 139–158.
- [50] X. Zuo, Z. Wang, Y. Liu, J. Shen, and H. Wang, "Lgadet: Lightweight anchor-free multispectral pedestrian detection with mixed local and global attention," *Neural Processing Letters*, vol. 55, no. 3, pp. 2935–2952, 2023.
- [51] Y. Cao, J. Bin, J. Hamari, E. Blasch, and Z. Liu, "Multimodal object detection by channel switching and spatial attention," in *Proceedings of the IEEE/CVF Conference on Computer Vision and Pattern Recognition Workshops*, 2023, pp. 403–411.
- [52] S. Hwang, J. Park, N. Kim, Y. Choi, and I. So Kweon, "Multispectral pedestrian detection: Benchmark dataset and baseline," in *Proceedings of the IEEE conference on computer vision and pattern recognition*, 2015, pp. 1037–1045.
- [53] J. Liu, S. Zhang, S. Wang, and D. N. Metaxas, "Multispectral deep neural networks for pedestrian detection," *arXiv preprint arXiv:1611.02644*, 2016.
- [54] D. König, M. Adam, C. Jarvers, G. Layher, H. Neumann, and M. Teutsch, "Fully convolutional region proposal networks for multi-pedestrian person detection," in *Proceedings of the IEEE conference on computer vision and pattern recognition workshops*, 2017, pp. 49–56.
- [55] C. Li, D. Song, R. Tong, and M. Tang, "Illumination-aware faster r-cnn for robust multispectral pedestrian detection," *Pattern Recognition*, vol. 85, pp. 161–171, 2019.
- [56] D. Guan, Y. Cao, J. Yang, Y. Cao, and M. Y. Yang, "Fusion of multispectral data through illumination-aware deep neural networks for pedestrian detection," *Information Fusion*, vol. 50, pp. 148–157, 2019.

- [57] C. Li, D. Song, R. Tong, and M. Tang, "Multispectral pedestrian detection via simultaneous detection and segmentation," in *British Machine Vision Conference (BMVC)*, 2018.
- [58] K. Zhou, L. Chen, and X. Cao, "Improving multispectral pedestrian detection by addressing modality imbalance problems," in *Computer Vision—ECCV 2020: 16th European Conference, Glasgow, UK, August 23–28, 2020, Proceedings, Part XVIII 16*. Springer, 2020, pp. 787–803.
- [59] Q. Li, C. Zhang, Q. Hu, H. Fu, and P. Zhu, "Confidence-aware fusion using dempster-shafer theory for multispectral pedestrian detection," *IEEE Transactions on Multimedia*, 2022.
- [60] Y. Sun, W. Zuo, and M. Liu, "Rtfnnet: Rgb-thermal fusion network for semantic segmentation of urban scenes," *IEEE Robotics and Automation Letters*, vol. 4, no. 3, pp. 2576–2583, 2019.
- [61] Z. Huang, X. Wang, L. Huang, C. Huang, Y. Wei, and W. Liu, "Ccnnet: Criss-cross attention for semantic segmentation," in *Proceedings of the IEEE/CVF international conference on computer vision*, 2019, pp. 603–612.
- [62] S. S. Shivakumar, N. Rodrigues, A. Zhou, I. D. Miller, V. Kumar, and C. J. Taylor, "Pst900: Rgb-thermal calibration, dataset and segmentation network," in *2020 IEEE international conference on robotics and automation (ICRA)*. IEEE, 2020, pp. 9441–9447.
- [63] X. Hu, K. Yang, L. Fei, and K. Wang, "Acnet: Attention based network to exploit complementary features for rgbd semantic segmentation," in *2019 IEEE International conference on image processing (ICIP)*. IEEE, 2019, pp. 1440–1444.
- [64] S. Zhao and Q. Zhang, "A feature divide-and-conquer network for rgb-t semantic segmentation," *IEEE Transactions on Circuits and Systems for Video Technology*, 2022.
- [65] Y. Fu, Q. Chen, and H. Zhao, "Cgfnnet: cross-guided fusion network for rgb-thermal semantic segmentation," *The Visual Computer*, vol. 38, no. 9, pp. 3243–3252, 2022.
- [66] W. Zhou, S. Dong, C. Xu, and Y. Qian, "Edge-aware guidance fusion network for rgb-thermal scene parsing," in *Proceedings of the AAAI conference on artificial intelligence*, vol. 36, no. 3, 2022, pp. 3571–3579.
- [67] P. Li, J. Chen, B. Lin, and X. Xu, "Residual spatial fusion network for rgb-thermal semantic segmentation," *arXiv preprint arXiv:2306.10364*, 2023.
- [68] Y. Wang, G. Li, and Z. Liu, "Sgfnnet: semantic-guided fusion network for rgb-thermal semantic segmentation," *IEEE Transactions on Circuits and Systems for Video Technology*, 2023.
- [69] H. Zhang, E. Fromont, S. Lefevre, and B. Avignon, "Multispectral fusion for object detection with cyclic fuse-and-refine blocks," in *2020 IEEE International conference on image processing (ICIP)*. IEEE, 2020, pp. 276–280.
- [70] X. Jia, C. Zhu, M. Li, W. Tang, and W. Zhou, "Llvp: A visible-infrared paired dataset for low-light vision," in *Proceedings of the IEEE/CVF international conference on computer vision*, 2021, pp. 3496–3504.
- [71] Y. Sun, W. Zuo, P. Yun, H. Wang, and M. Liu, "Fuseseq: Semantic segmentation of urban scenes based on rgb and thermal data fusion," *IEEE Transactions on Automation Science and Engineering*, vol. 18, no. 3, pp. 1000–1011, 2020.
- [72] Q. Zhang, S. Zhao, Y. Luo, D. Zhang, N. Huang, and J. Han, "Abmdrnet: Adaptive-weighted bi-directional modality difference reduction network for rgb-t semantic segmentation," in *Proceedings of the IEEE/CVF Conference on Computer Vision and Pattern Recognition*, 2021, pp. 2633–2642.
- [73] W. Zhou, X. Lin, J. Lei, L. Yu, and J.-N. Hwang, "Mffnet: Multiscale feature fusion and enhancement network for rgb-thermal urban road scene parsing," *IEEE Transactions on Multimedia*, vol. 24, pp. 2526–2538, 2021.
- [74] W. Zhou, S. Dong, J. Lei, and L. Yu, "Mtanet: Multitask-aware network with hierarchical multimodal fusion for rgb-t urban scene understanding," *IEEE Transactions on Intelligent Vehicles*, vol. 8, no. 1, pp. 48–58, 2022.
- [75] Z. Guo, X. Li, Q. Xu, and Z. Sun, "Robust semantic segmentation based on rgb-thermal in variable lighting scenes," *Measurement*, vol. 186, p. 110176, 2021.
- [76] F. Deng, H. Feng, M. Liang, H. Wang, Y. Yang, Y. Gao, J. Chen, J. Hu, X. Guo, and T. L. Lam, "Feanet: Feature-enhanced attention network for rgb-thermal real-time semantic segmentation," in *2021 IEEE/RSJ International Conference on Intelligent Robots and Systems (IROS)*. IEEE, 2021, pp. 4467–4473.
- [77] W. Zhou, J. Liu, J. Lei, L. Yu, and J.-N. Hwang, "Gmnet: Graded-feature multilabel-learning network for rgb-thermal urban scene semantic segmentation," *IEEE Transactions on Image Processing*, vol. 30, pp. 7790–7802, 2021.
- [78] S. Yi, J. Li, X. Liu, and X. Yuan, "Ccaffmnet: Dual-spectral semantic segmentation network with channel-coordinate attention feature fusion module," *Neurocomputing*, vol. 482, pp. 236–251, 2022.
- [79] W. Zhou, Y. Lv, J. Lei, and L. Yu, "Embedded control gate fusion and attention residual learning for rgb-thermal urban scene parsing," *IEEE Transactions on Intelligent Transportation Systems*, 2023.
- [80] G. Li, Y. Wang, Z. Liu, X. Zhang, and D. Zeng, "Rgb-t semantic segmentation with location, activation, and sharpening," *IEEE Transactions on Circuits and Systems for Video Technology*, vol. 33, no. 3, pp. 1223–1235, 2022.
- [81] S. Zheng, J. Lu, H. Zhao, X. Zhu, Z. Luo, Y. Wang, Y. Fu, J. Feng, T. Xiang, P. H. Torr *et al.*, "Rethinking semantic segmentation from a sequence-to-sequence perspective with transformers," in *CVPR*, 2021, pp. 6881–6890.
- [82] A. Vaswani, N. Shazeer, N. Parmar, J. Uszkoreit, L. Jones, A. N. Gomez, Ł. Kaiser, and I. Polosukhin, "Attention is all you need," *Advances in neural information processing systems*, vol. 30, 2017.
- [83] H. Chen, Y. Li, and D. Su, "Multi-modal fusion network with multi-scale multi-path and cross-modal interactions for rgb-d salient object detection," *Pattern Recognition*, vol. 86, pp. 376–385, 2019.
- [84] H. Chen and Y. Li, "Three-stream attention-aware network for rgb-d salient object detection," *TIP*, vol. 28, no. 6, pp. 2825–2835, 2019.
- [85] N. Liu, N. Zhang, and J. Han, "Learning selective self-mutual attention for rgb-d saliency detection," in *CVPR*, 2020, pp. 13 756–13 765.
- [86] K. Fu, D.-P. Fan, G.-P. Ji, Q. Zhao, J. Shen, and C. Zhu, "Siamese network for rgb-d salient object detection and beyond," *TPAMI*, vol. 44, no. 9, pp. 5541–5559, 2021.
- [87] G. Wang, C. Li, Y. Ma, A. Zheng, J. Tang, and B. Luo, "Rgb-t saliency detection benchmark: Dataset, baselines, analysis and a novel approach," in *IGTA*. Springer, 2018, pp. 359–369.
- [88] Z. Tu, T. Xia, C. Li, Y. Lu, and J. Tang, "M3s-nir: Multi-modal multi-scale noise-insensitive ranking for rgb-t saliency detection," in *MIPR*. IEEE, 2019, pp. 141–146.
- [89] Z. Tu, T. Xia, C. Li, X. Wang, Y. Ma, and J. Tang, "Rgb-t image saliency detection via collaborative graph learning," *TMM*, vol. 22, no. 1, pp. 160–173, 2019.
- [90] Q. Zhang, N. Huang, L. Yao, D. Zhang, C. Shan, and J. Han, "Rgb-t salient object detection via fusing multi-level cnn features," *IEEE Transactions on Image Processing*, vol. 29, pp. 3321–3335, 2019.
- [91] Z. Tu, Z. Li, C. Li, Y. Lang, and J. Tang, "Multi-interactive dual-decoder for rgb-thermal salient object detection," *IEEE Transactions on Image Processing*, vol. 30, pp. 5678–5691, 2021.
- [92] Z. Tu, Y. Ma, Z. Li, C. Li, J. Xu, and Y. Liu, "Rgbd salient object detection: A large-scale dataset and benchmark," *TMM*, 2022.
- [93] W. Zhou, Y. Zhu, J. Lei, R. Yang, and L. Yu, "Lsnet: Lightweight spatial boosting network for detecting salient objects in rgb-thermal images," *IEEE Transactions on Image Processing*, vol. 32, pp. 1329–1340, 2023.
- [94] B. Abidi, "Iris thermal/visible face database," *IEEE OTCBVS WS Series Bench.*, pp. <http://vcipl-okstate.org/pbvs/bench/>, accessed 2020-06-09.
- [95] J. Deng, J. Guo, X. Niannan, and S. Zafeiriou, "Arcface: Additive angular margin loss for deep face recognition," in *CVPR*, 2019.
- [96] M. Kim, A. K. Jain, and X. Liu, "Adaface: Quality adaptive margin for face recognition," in *Proceedings of the IEEE/CVF conference on computer vision and pattern recognition*, 2022, pp. 18 750–18 759.